

MATERIALS SCIENCE

The origin and stability of nanostructural hierarchy in crystalline solids

S. Meher^{1*}, L. K. Aagesen^{2*}, M. C. Carroll³, T. M. Pollock⁴, L. J. Carroll^{1†}

The structural hierarchy exhibited by materials on more than one length scale can play a major part in determining bulk material properties. Understanding the hierarchical structure can lead to new materials with physical properties tailored for specific applications. We have used a combined experimental and phase-field modeling approach to explore such a hierarchical structure at nanoscale for enhanced coarsening resistance of ordered γ' precipitates in an experimental, multicomponent, high-refractory nickel-base superalloy. The hierarchical microstructure formed experimentally in this alloy is composed of a γ matrix with γ' precipitates that contain embedded, spherical γ precipitates, which do not directionally coarsen during high-temperature annealing but do delay coarsening of the larger γ' precipitates. Chemical mapping via atom probe tomography suggests that the supersaturation of Co, Ru, and Re in the γ' phase is the driving force for the phase separation, leading to the formation of this hierarchical microstructure. Representative phase-field modeling highlights the importance of larger γ' precipitates to promote stability of the embedded γ phase and to delay coarsening of the encompassing γ' precipitates. Our results suggest that the hierarchical material design has the potential to influence the high-temperature stability of precipitate strengthened metallic materials.

INTRODUCTION

Hierarchical microstructures, defined as having key features spanning from the nanoscale to the microscale, have recently been of interest for improved high-temperature creep resistance in Fe-base (1, 2), Ti-base (3), and Ni-base alloys (4). The characterization of these hierarchical structures, created by phase transformations, is essential for establishing a fundamental understanding of their stability. Long-term morphological stability of the ordered γ' phase, which provides potent high-temperature strengthening in aluminum-rich nickel-base superalloys (5), would be highly beneficial for structural materials requiring high temperatures and long design lifetimes. Specific needs would include emerging fossil and solar energy applications (6, 7).

The γ' precipitates in nickel-base alloys naturally coarsen at elevated temperatures, eventually degrading the optimized mechanical properties (5, 8). A typical γ - γ' microstructure consists of ordered γ' precipitates in a continuous, disordered γ matrix. Variations in this structure are occasionally observed, however, such as an inverted microstructure in which γ precipitates reside in a continuous γ' phase (9–12) as well as a hierarchical microstructure consisting of a γ matrix with γ' precipitates embedded with still finer-scale γ particles (4, 13–15), as shown in Fig. 1.

For hierarchical microstructures, delayed coarsening of the encompassing γ' precipitates has been reported during the time in which the embedded nanoscale γ precipitates enlarge (4, 13). In these relatively high lattice misfit hierarchical superalloys, the tiny γ precipitates coarsen into raft-like structures that eventually reach the edges of the encompassing γ' precipitates and subdivide the larger cuboidal γ' precipitates (4, 14, 15). This chemical phase separation of the individual larger-sized γ' precipitates ultimately results in the splitting of γ' precipitates with continued high-temperature exposure. This subdivision initially inhibits the overall coarsening of γ' precipitates but is short lived as classical

coarsening resumes once the embedded nanoscale γ precipitates are no longer present (4). Elemental diffusion from the γ' -embedded γ precipitates to the continuous γ matrix maintains the equilibrium γ volume fraction. This effect in Ni-Al-Ti alloys has been rationalized on the basis of an abnormal γ' solvus line leading to off-stoichiometric γ' phase compositions during thermal treatment where γ precipitate nucleation occurs within the well-formed supersaturated γ' precipitates (13).

Kinetic modeling of the evolution of these atypical microstructures is limited. Phase-field modeling (16–18) of an inverse Ni-base superalloy, where γ precipitates reside in a continuous γ' matrix phase, is consistent with experimental observations (10, 11) of classical coarsening of the γ precipitates. There is no similar published work, however, regarding a hierarchically structured γ - γ' alloy.

Of particular interest is finding a chemical and thermal pathway for enhancing resistance to coarsening and subsequently improving high-temperature alloy stability. This is potentially achievable by delaying the coarsening process of the large (micrometer-scale) γ' precipitates through both stabilization and inhibition of coalescence of the embedded nanoscale γ precipitates. Here, the stability of a hierarchal

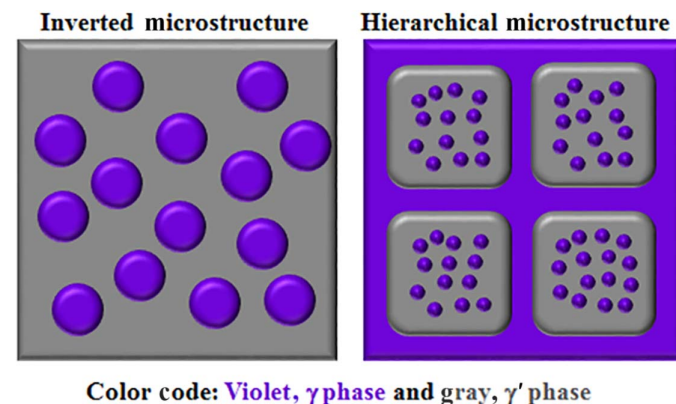


Fig. 1. A schematic of an inverted and a hierarchical microstructure observed in Ni-base superalloys. The violet and gray regions represent the γ and γ' phase, respectively.

¹Materials Science and Engineering Department, Idaho National Laboratory, Idaho Falls, ID 83415, USA. ²Fuels Modeling and Simulation, Idaho National Laboratory, Idaho Falls, ID 83415, USA. ³Federal-Mogul Powertrain, Plymouth, MI 48170, USA. ⁴Materials Department, University of California Santa Barbara, Santa Barbara, CA 93106, USA.

*Corresponding author. Email: subhashish.meher@inl.gov (S.M.); larry.aagesen@inl.gov (L.K.A.)

†Present address: University of Michigan, Ann Arbor, MI 48109, USA.

microstructure is considered for an experimental γ - γ' nickel alloy with a low magnitude of γ - γ' lattice mismatch. Atom probe tomography (APT) is used to identify the solute species responsible for the supersaturation of γ' precipitates that subsequently drives the formation of the hierarchical microstructure in a multicomponent nickel alloy. The main objective is to explore the chemical and microstructural factors contributing to the stability of a hierarchical γ - γ' microstructure.

RESULTS

Initial microstructure at 800°C

The as-cast samples of a Ni-13.6Al-7.6Co-3.0Ta-1.5W-5.9Ru-1.3Re [atomic % (at %)] experimental alloy (designated alloy F-11) were homogenized at 1285°C for 12 hours and then air-cooled. Nickel-base superalloys solidify dendritically with the dendritic regions solidifying first while rejecting solute into the interdendritic region and resulting in elemental segregation between the two regions (5, 19, 20). Low-magnification images capturing both the dendritic and interdendritic regions in F-11 are shown in fig. S1. The air-cooled samples were isothermally annealed at 800°C, which produced different microstructures in the dendritic and interdendritic regions. Figure 2A is a bright-field transmission electron microscopy (TEM) micrograph from the interdendritic region after isothermally annealing for 1500 hours that shows a monomodal distribution of γ precipitates, with approximately 20 to 25% volume fraction and an average radius of 10 nm, within a γ' matrix. Selected area diffraction patterns of this area in the [001] zone axis revealed the principal spots of the face-centered cubic crystal structure, along with superlattice spots corresponding to the γ' matrix. Since diffraction information solely from γ precipitates is not possible from TEM, a typical $\gamma + \gamma'$ diffraction pattern along the [001] zone axis with no other additional spots is consistent with the presence of these two phases.

A dark-field TEM micrograph from the dendritic region after annealing for 25 hours is shown in Fig. 2B and reveals a different microstructure, in which nanoscale γ precipitates are observed within secondary γ' precipitates that are 100 to 150 nm in radius within a continuous γ matrix. The embedded nanoscale phase is γ , based on the similarity of the γ and γ' phase compositions in the dendritic and interdendritic regions (table S1) along with the elemental partitioning between the embedded precipitate and the encompassing γ' precipitate (also evident from table S1). These embedded nanoscale γ precipitates were not observed in the microstructure following air cooling from solution; instead, their presence is first noted following annealing at 800°C. Fine γ' precipitates, identified on the basis of composition from APT partitioning data, in the γ matrix channels were also present following homogenization and air cooling. In an effort to understand the evolution of the hierarchical microstructure, the dendritic region will be the focus of this study. For comparison, the microstructure within the dendritic region after annealing at 1000°C for 500 hours is shown in a dark-field TEM micrograph in Fig. 2C. A γ' precipitate several hundred nanometers in diameter is surrounded by a continuous γ matrix and does not exhibit the presence of embedded γ precipitates.

The APT-determined local compositions within the dendritic and interdendritic regions of experimental alloy F-11 after isothermal annealing at 800°C for 1500 hours are included in table S1. To represent alloy F-11 via simulation, Fig. 2 (D and E) shows Thermo-Calc plots of the equilibrium γ' volume fraction as a function of temperature, indicating a decrease in volume fraction at temperatures below 840°C. While it is challenging to create a phase diagram for more complex multicomponent systems, in this case, a decreasing γ' volume fraction trend with temperature results in interesting phase decomposition processes, as previously reported for simpler Ni-base alloys (13). Figure 2E predicts an approximately 4% decrease in γ' volume fraction at 800°C

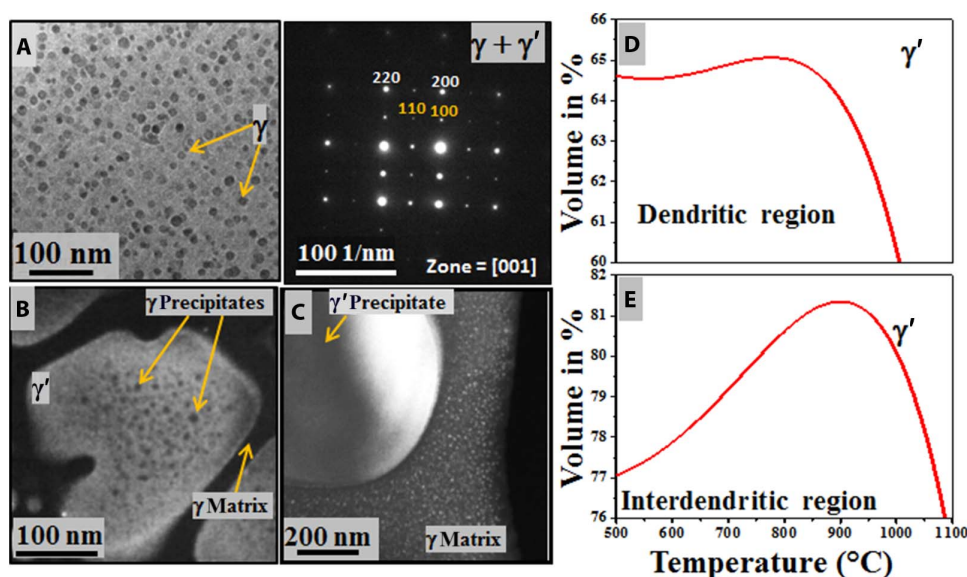


Fig. 2. TEM identifies an inverted and a hierarchical microstructure observed in Ni-base superalloys. (A) Bright-field TEM micrograph showing the homogeneous distribution of γ precipitates in a continuous γ' matrix in the interdendritic region after annealing at 800°C for 1500 hours. A diffraction pattern along the [001] zone axis is consistent with that of a typical $\gamma + \gamma'$ diffraction pattern and does not contain additional spots, again consistent with the γ and γ' phases. (B) A dark-field TEM micrograph from an area within the dendritic region showing the presence of fine, embedded γ precipitates (darker region) within the secondary γ' precipitates after annealing at 800°C for 25 hours and (C) a dark-field TEM micrograph of a secondary γ' precipitate, with no evidence of γ' phase separation, in a γ matrix after annealing at 1000°C for 500 hours. Thermo-Calc plots of the volume fraction of γ' precipitates as a function of temperature for an alloy composition matching that in the (D) dendritic and (E) interdendritic regions.

from the peak and an equilibrium volume fraction of γ precipitates in the interdendritic region of 20%, which is consistent with experimental observations. The TEM results suggest that the simulated plots in Fig. 2 (D and E) may slightly underestimate the absolute γ' volume fraction compared to that observed experimentally. Currently, there is no set of direct experimental results to validate the simulated decrease in γ' volume fraction with temperature.

Evolution of hierarchical microstructure

Figure 3A shows the size evolution of the nanoscale γ precipitates embedded in γ' precipitates during isothermal annealing at 800°C. The γ' precipitate radius is approximately 100 nm after air cooling from the solution temperature, and the equilibrium γ' volume fraction, determined from a specimen exposed to an extended anneal, is approximately 60%. The precipitates are initially irregular in shape, evolving during annealing into a more regular morphology. Despite this, they coarsen to a shape that is neither fully spherical nor cuboidal and continue to exhibit no spatial correlation, thus signifying a low γ - γ' lattice mismatch magnitude at 800°C. Simultaneous with volumetric coarsening, the γ precipitates undergo continuous dissolution and are no longer present within the γ' precipitates after 500 hours. The evolution of embedded γ precipitate radius size and volume fraction has not been quantified. While it is expected that the secondary γ' precipitates should follow the Lifshitz-Slyozov-Wagner (LSW) coarsening after 500 hours of annealing, the coarsening rate was found to be much slower, as shown in fig. S2. The tertiary γ' precipitates, present as fine, nanoscale precipitates in the matrix channels, selectively coarsen and then dissolve in the wide and narrow channels, respectively, during annealing at 800°C for 1500 hours, ultimately resulting in a unimodal precipitate distribution as shown in fig. S3.

For comparison, Fig. 3B shows the temporal evolution in the same alloy at 1000°C, in which there exists a more typical, bimodal γ - γ' microstructure and no evidence of a hierarchical structure. The radius size evolution and coarsening kinetics of the secondary γ' precipitates at 1000°C are provided in fig. S4. Figure 3C is a plot of the mean secondary γ' radius as a function of annealing time that enables a comparison of the evolution of the average γ' precipitate radius at 800° and 1000°C. While the secondary γ' precipitates follow classical LSW coarsening at 1000°C, exposures at 800°C result in these precipitates initially undergoing a decrease in radius size as the coarsening is delayed until approximately 500 hours. By 500 hours, complete dissolution of embedded γ precipitates has occurred, as shown in Fig. 3A, and coarsening resumes such that the γ' precipitate radius steadily increases in size. The tertiary γ' precipitates present in the matrix channels also coarsen at 1000°C until a unimodal precipitate distribution exists at 1000 hours. While the hierarchical microstructure definitely delays the coarsening process possibly up to 500 hours; ideally, this structure should not contribute to the presently observed reduced coarsening rate of secondary γ' precipitates after 500 hours (fig. S2). In addition, it is unknown whether selective coarsening and dissolution of tertiary precipitates (fig. S3) can affect the observed reduced coarsening rate of secondary γ' precipitates after 500 hours of annealing.

The compositions of the γ' precipitates in the air-cooled condition and following isothermal annealing at 800°C are quantified in table S2. All the samples in this study were air-cooled from the homogenization temperature. The amount of γ -forming elements, Ru, Co, and Re, in the γ' phase is higher in the air-cooled condition compared with those after annealing at 800°C. This supersaturation of the γ' phase with γ -forming solutes is consistent with the decrease in the equilibrium volume fraction

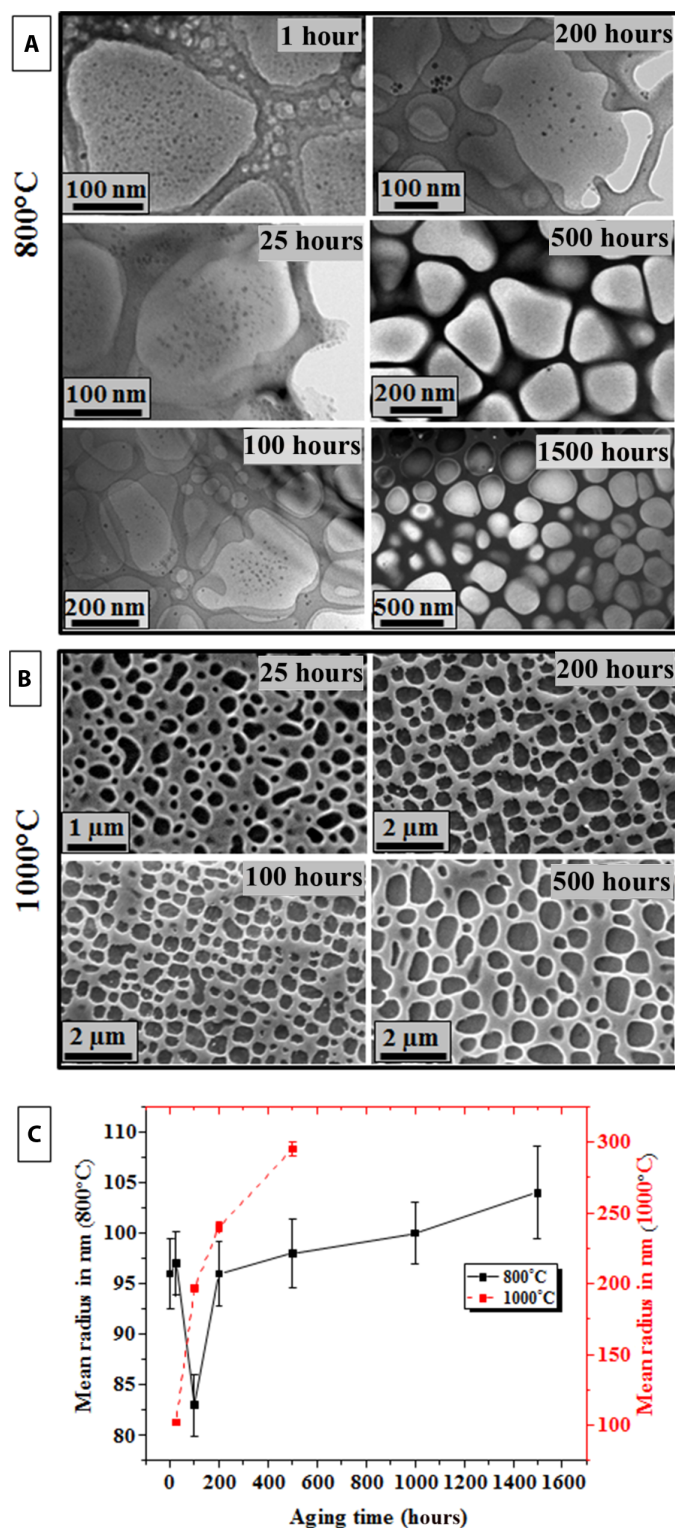


Fig. 3. Comparative temporal evolution of secondary γ' precipitates in hierarchical and regular microstructure in Ni-base superalloy. (A) TEM micrographs show the evolution of nanoscale γ precipitates embedded in γ' precipitates following isothermal annealing at 800°C. (B) Scanning electron microscopy (SEM) micrographs show the evolution of γ' precipitates embedded in a γ matrix following isothermal annealing at 1000°C. (C) Plot showing the mean γ' precipitate radius as a function of annealing time with (800°C) and without (1000°C) the presence of embedded nanoscale γ precipitates.

of γ' phase simulated via Thermo-Calc in Fig. 2D. Consequently, the possibility of a hierarchical metastable equilibrium microstructure through the nucleation of nanoscale γ precipitates arises, as is experimentally observed.

Since multiple γ and γ' phase-forming solutes are present in this alloy, the individual solute behavior responsible for γ precipitates nucleating and growing within a γ' precipitate has been further studied by examining the nanoscale diffusion behavior at an early stage of annealing. Figure 4A shows a bright-field TEM image of a sample annealed for 1 hour at 800°C. The gray rim surrounding the larger γ' precipitates is an artifact arising because of under- or overfocusing of the microscope, such that the embedded γ precipitates are visible. This rim is not present in the APT results. The nanoscale γ precipitates, identified as γ on the basis of on the APT solute partitioning trends, have an average radius of 2 to 3 nm and are mostly located away from the periphery of the γ' precipitate, forming a precipitate-free zone (PFZ) near the interface. Figure 4B shows an APT reconstruction, after 1 hour at 800°C, in which the 12 at % Al isosurface reveals γ precipitates embedded in a γ' precipitate with a PFZ width of approximately 15 nm. The cylindrical region of interest (ROI), 35 nm in length and 20 nm in diameter, was placed at the interface of a γ' precipitate and the γ matrix and encompassed the entire PFZ. The corresponding one-dimensional (1D) compositional analysis along the length of the ROI cylinder is

shown in Fig. 4 (C and D). Figure 4C includes the compositional variations of only the fast-diffusing elements, Co, Ru, and Al. The depletion of the γ precipitate-forming elements, Ru and Co, in the PFZ near the γ - γ' interface is evident from the proxigram, suggesting that they are rejected across the interface toward the γ matrix. The compositional analysis of slow-diffusing elements, Re and W, in Fig. 4D does not show any apparent depletion or enrichment, which is consistent with the sluggish diffusivity of these solutes. However, Ta does show a slight enrichment at the PFZ possibly due to its higher diffusivity in Ni as compared with that of Re and W in Ni. These elements, therefore, contribute to slowing the coarsening and dissolution of nanoscale γ precipitates.

Phase-field modeling

To study the effect of lattice misfit and initial microstructure at 800°C on the morphological evolution of hierarchical microstructures, we have used phase-field methods to simulate the microstructural evolution. The complexity of the experimental multicomponent alloy's free energy landscape renders it unwieldy to accurately simulate the full seven-component system. In addition, some physical parameters needed to parameterize the phase-field model are not known for the experimental alloy. For these reasons, a simplified model based on the well-characterized Ni-Al binary system was adopted with physical parameters such as the

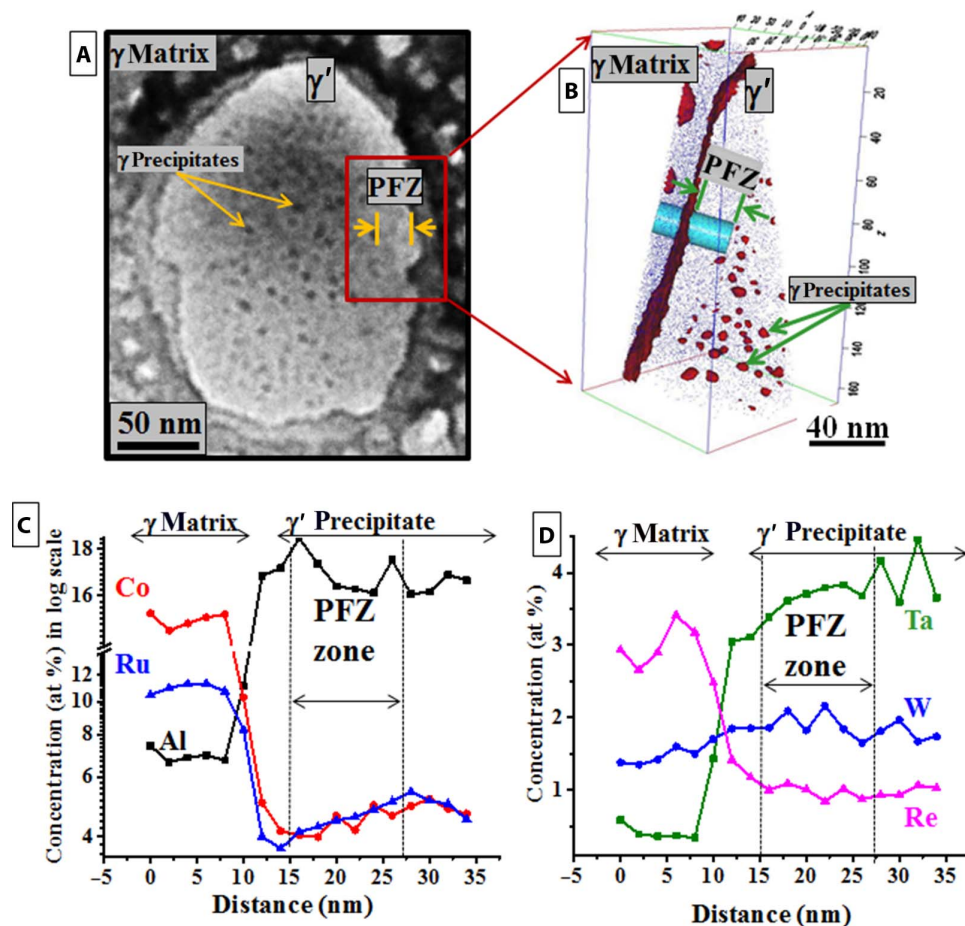


Fig. 4. Atomic scale rendition of chemical origin of hierarchical microstructure Ni-base superalloy. (A) Bright-field TEM image after annealing at 800°C for 1 hour that shows a PFZ within γ' precipitates close to secondary γ - γ' matrix interface. (B) Corresponding APT reconstruction, created using 8 at % Ru isosurface (red), showing the PFZ zone and relevant ROI for chemical analysis. A 1D line profile, corresponding to the ROI in (B), shows the distribution of fast-diffusing (C) and slow-diffusing (D) solutes within the PFZ.

diffusion coefficient and interfacial energy modified for the F-11 alloy (see Materials and Methods for details).

The initial simulation condition consists of a single γ' precipitate of 100 nm in diameter with composition Ni-22.7 Al (at %) in a matrix of Ni-13 Al (at %) and is shown in Fig. 5A. The γ' precipitate contains a 10% volume fraction of γ precipitates inside a 15-nm PFZ. Since the experimental misfit values have not been determined, Fig. 5 (B to D) shows the simulation results for the γ - γ' microstructure after 2500 hours at 800°C for various magnitudes of lattice misfit. For all investigated lattice misfits, the γ precipitates embedded inside the single encompassing γ' precipitate maintain a spherical shape while coarsening. The variations in magnitude of the lattice misfit have minimal influence on the embedded precipitate evolution. At 2500 hours, the volume fraction of embedded γ precipitates within the γ' precipitate decreases to approximately 7.5%. As shown in Fig. 6 (A and B), the volume fraction of the embedded γ precipitates decreases with time, following a short period of increase during equilibration of the initial simulated conditions. The decrease in the embedded γ precipitate volume fraction occurs because of the diffusion of γ -forming Ni from the embedded γ precipitates to the γ' matrix, effectively transporting the γ phase from inside the γ' particles to the γ matrix and causing the γ' phase to shrink. This process is driven by the reduction of interfacial energy. At the same time, coarsening occurs for the embedded γ precipitates, causing the remaining precipitates located near the center of the precipitate to increase

in size (Fig. 5, B to D). Because the volume fraction of embedded γ precipitates is not conserved, the LSW assumptions for coarsening are not met, so it is not expected that the average embedded precipitate radius increases with $t^{1/3}$.

The simulations indicate that an appreciable amount of time is required to dissolve most of the γ precipitates inside a single γ' precipitate with an initial diameter of 100 and 200 nm, shown in Fig. 6 (A and B, respectively). The complete dissolution of the γ precipitates in a 100-nm precipitate occurs in nearly 2×10^4 hours, while the dissolution process in the larger precipitate is substantially slower. In contrast to the lattice misfit, the initial γ' precipitate radius has a substantial influence on the stability of the γ precipitates. An order of magnitude estimate for the time required for a diffusion-limited process to take place can be obtained using $t = x^2/D$, where x is the distance over which diffusion occurs. Assume that for the dissolution of the embedded γ precipitates, t is the time required for the embedded γ precipitates to dissolve, D is the diffusivity, (or in this case, 7.3×10^{-23} m²/s), and x is equal to the γ' particle radius. As an estimate, the D value used is from the coarsening kinetics of the inverted microstructure of the interdendritic region, although it is recognized that this value will differ because of the differing compositions. The details of the coarsening of γ precipitates in a γ' matrix in the interdendritic region during isothermal annealing at 800°C has been presented in the Supplementary Materials and fig. S7. Using this assumption, for the 100-nm γ' particle, $t = 9.5 \times 10^3$ hours, a

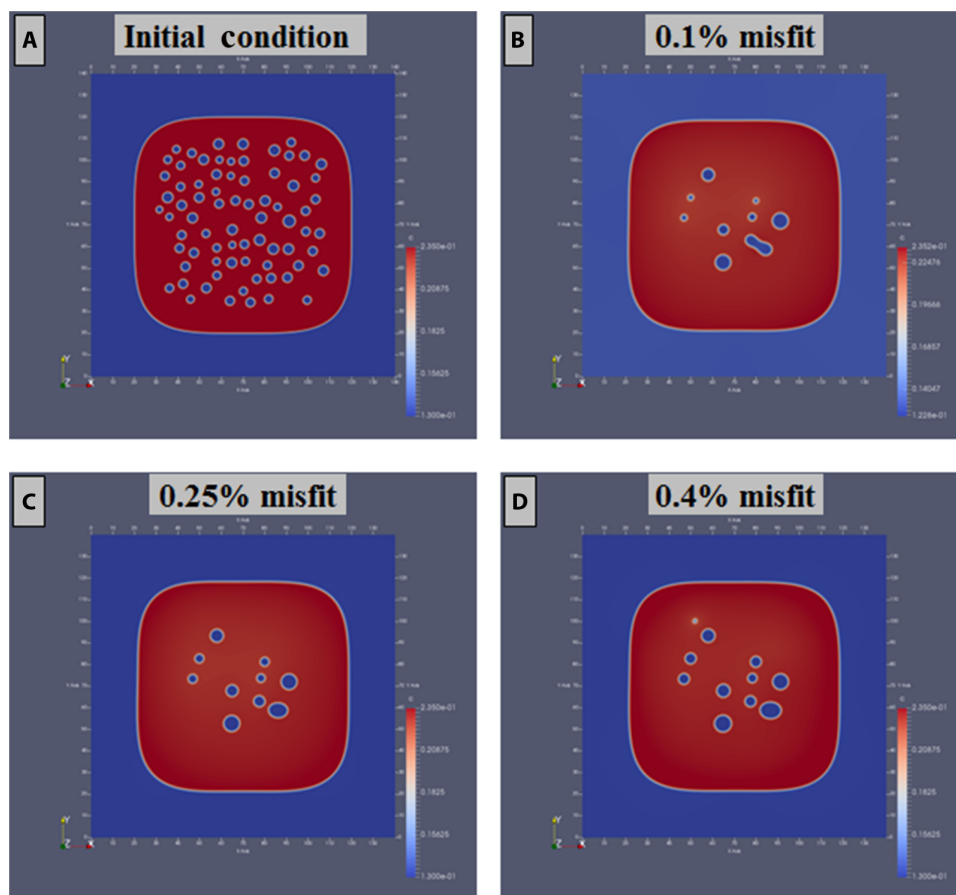


Fig. 5. The evolution of hierarchical microstructure, as determined by phase-field modeling, in Ni-base superalloy with variation in γ/γ' lattice misfit. (A) Initial condition for phase-field modeling of a 100-nm-diameter γ' precipitate with 10% of embedded γ precipitates at 800°C. The microstructural evolution during isothermal annealing at 800°C for 2500 hours for a given lattice misfit, 0.1% (B), 0.25% (C), and 0.4% (D).

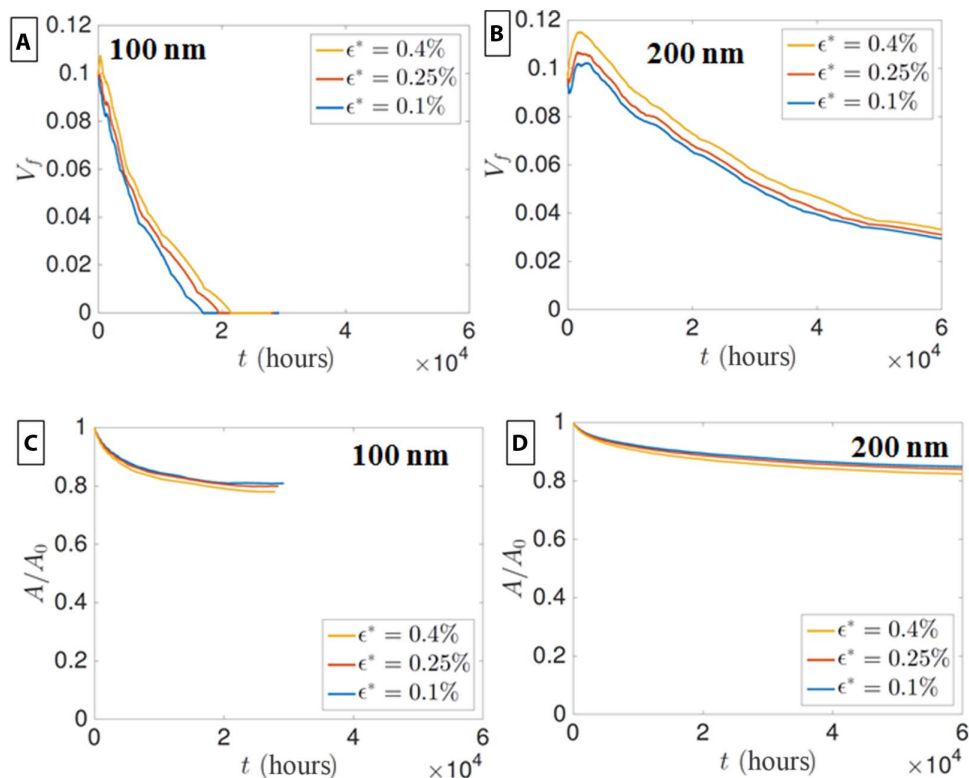


Fig. 6. The long-term stability of hierarchical microstructure as determined by phase-field modeling. Phase-field modeling results showing the reduction in volume fraction of γ precipitates within a γ' precipitate with an initial diameter of (A) 100 nm and (B) 200 nm and the change of area (A) of the encompassing secondary γ' precipitate relative to the initial area (A_0) for (C) 100-nm- and (D) 200-nm-diameter particles during coarsening at 800°C.

factor of approximately 2 lower than the value of 2×10^4 hours predicted by phase-field simulation for the time required for all the embedded γ precipitates to dissolve. For the 200-nm γ' particle, $t = 3.8 \times 10^4$ hours, in which case the simulations predict that the embedded γ particles are still present for $t > 6 \times 10^4$ hours. Thus, $t = x^2/D$ gives a lower bound for the time required for the embedded γ particles to dissolve. Since t increases in proportion to x^2 , increasing the γ' particle size greatly increases the time required for the embedded γ particles to dissolve and, therefore, contributes to the microstructural stability of the γ' particles.

Plots resulting from the phase-field modeling in Fig. 6 (C and D) show the change of area (A) of the encompassing secondary γ' precipitate relative to the initial area (A_0) for 100- and 200-nm-diameter particles, respectively, during coarsening at 800°C. The simulation results show that there is a decrease in the area of the secondary γ' precipitate that is not accompanied by a change in shape, indicating at least an initial period of shrinkage of γ' precipitate size due to a decrease in the volume fraction. The modeled decrease in precipitate size during coarsening is consistent with the experimental observations at 800°C for annealing times as long as 200 hours, as is shown graphically in Fig. 3C.

DISCUSSION

The specific combination of composition and processing resulted in atypical microstructures in both the interdendritic and dendritic regions of the investigated experimental alloy. The cooling rate created a meta-

stable microstructure that had not yet reached equilibrium during isothermal annealing at 800°C and was able to more quickly reach equilibrium at 1000°C. Previous work on simpler Ni-Al and Ni-Al-Ti alloys found that Ni, the only γ -forming solute in these alloys, was responsible for the γ' phase splitting (4, 11, 13). For the more compositionally complex alloy investigated here, the APT-quantified relative composition change between the homogenized condition and after annealing at 800°C suggests that the γ -forming elements Ru, Co, and Re are responsible for the nucleation of embedded γ precipitates and for the formation of a hierarchical microstructure.

The idea that alloy composition, specifically Ru, Co, and Re, contributes to the development of hierarchical microstructures suggests that there may be a wider set of elements capable of promoting this type of microstructure. Recent work has found that the combination of strong γ' partitioning and low interdiffusion rates stemming from additions of Pt to a nickel superalloy result in a substantially reduced precipitate coarsening rate and improved higher-temperature stability (21). The current study in combination with that of Van Sluytman *et al.* (21) suggests that the coarsening resistance of hierarchical microstructures may also benefit from Pt additions to their base compositions, further improving not only the long-term stability but also the temperature capability. The phase-field modeling of the hierarchical microstructure used the effective D value, as determined from coarsening kinetics of γ precipitates in the interdendritic region and presented in table S3, and showed the stability of γ precipitates for times up to 24,000 hours. The observed complete dissolution of γ precipitates inside γ' precipitates within 500 hours of annealing at 800°C

is indicative of a higher effective diffusivity in the dendritic region than was estimated.

The directional alignment of the nanoscale γ precipitates in hierarchical microstructures has been previously observed (4, 13). There, the aligned nanoscale γ precipitates coalesced into rafts and split the γ' precipitates. In contrast, in the present work, the spherical morphology of the nanoscale γ precipitates persisted, as observed experimentally and predicted by phase-field modeling, and rafting and splitting of the γ' precipitates did not occur. This was initially somewhat unexpected but may be reasonably explained. For materials with cubic symmetry, the morphology of a particle is a function of the dimensionless parameter $L = C_{44}(\epsilon^*)^2/l\sigma$, where C_{44} is an element of the elastic stiffness tensor, ϵ^* is the misfit strain, σ is the interfacial energy, and l is the characteristic size of the particle (22). For a spherical particle, l is equal to the particle radius. The parameter L is the ratio of characteristic elastic to interfacial energies. When $L < 1$, the characteristic elastic energy is small relative to the characteristic interfacial energy, and the morphology is dominated by interfacial energy, resulting in spherical morphologies (circular in 2D). In the present work, the embedded γ particles are quite small, less than 15 nm in radius in experimental observation, and possibly slightly larger at the very late stages of simulation. For a 15-nm-radius particle, even for the largest misfit strain considered here ($\epsilon^* = 0.4\%$), $L = 0.52$ and results in a spherical morphology. The spherical shape results in a substantial reduction in magnitude of the stress fields that would otherwise lead to particle alignment, accounting for the lack of directional alignment in the present system. This is in contrast to previously conducted work (16) where elongated, aligned precipitates were observed, which reasonably results from the fact that the γ - γ' interfacial energy in binary Ni-Al alloys is much smaller [10 mJ/m² (23)] than the calculated value for the present system (46.8 mJ/m²). This leads to $L = 2.4$ for a particle of an equivalent characteristic size of 15 nm and results in the elastic energy dominating the morphology. In high-misfit superalloys, elongation and directional alignment are expected for large L and is thus a function of elastic constants, interfacial energy, and characteristic particle size. It should be noted that the phase-field model shows the expected elongated shape for γ' particles in a γ matrix when the interfacial energy is that of the Ni-Al binary system, 10 mJ/m², with a misfit strain of 0.327%. In these 2D simulations, the transition between cuboidal and elongated morphology happens at an L of greater than 5, which is in agreement with the value of 5.6 found by Su and Voorhees (22).

The solute supersaturation-induced phase separation distributes the equilibrium volume fraction of the γ phase in two morphological variants in the hierarchical microstructure: nanoscale precipitates present within the larger γ' precipitates and as a continuous matrix. As the γ' phase precipitated during air cooling following homogenization, limited diffusion occurs, and equilibrium is not yet reached; subsequent time at 800°C enables additional diffusion and allows the microstructure to evolve. It is evident from table S2 that larger amounts of the γ -forming elements, Co, Ru, and Re, are initially present in the γ' precipitates, from diffusion processes leading to the formation of embedded nanoscale γ precipitates. While the equilibrium compositions are expected to be the same, the free energy of the nanoscale γ precipitates is expected to be higher because of their high radius of curvature (24). Continued thermal exposure drives to lower the free energy by eliminating the high-curvature, γ precipitate- γ' precipitate interfaces, leading to the dissolution of the γ precipitates. Interparticle coarsening and coalescence of γ precipitates may also be

occurring simultaneously, which affects the microstructure but does not result in a changing volume fraction.

Ultimately, determining mechanisms with a higher propensity for retaining the metastable nanoscale precipitates would be ideal, as the presence of this nanoscale distribution has been found not only to strengthen the γ' phase (4, 25, 26) but also to inhibit the coarsening of the secondary precipitates, as is observed here and in other published work (4, 13). The present study provides suggestions for manipulation of the metastable hierarchical microstructure through the interfacial energy, solute diffusivity, γ' precipitate size, and supersaturation of specific γ former solute to enhance its stability.

In the case of the interfacial energy, one method to improve stability is through a reduction in the γ - γ' interfacial energy and, ultimately, the coarsening coefficient. The interfacial energy of the experimental alloy was estimated to be 47 mJ/m², but there is evidence of interfacial energies as low as 3 to 5 mJ/m² in γ - γ' Ni-base alloys (27). Since the coarsening/dissolution kinetics are nearly proportional to the interfacial energy, it is expected that the stability of γ precipitates can be enhanced to achieve 5 to 10 times longer durations, provided that optimum elastic strain is maintained to avoid directional coarsening. The driving force for dissolution of γ precipitates based on their nanoscale size will still exist.

The solute diffusivity can also impart reduced transformation kinetics through slower movement of refractory elements, further enhancing the stability of the embedded nanoscale precipitates. In addition, phase-field modeling also identifies the role of the initial γ' radius size on the stability of this phase-separated microstructure. This aspect directs the initial thermal treatment to obtain coarser γ' precipitates, after determining the optimum size that avoids degradation of the mechanical properties. Last, there is a role for alloy chemistry in influencing the extent of supersaturation; systems with greater degrees of solute supersaturation will impart a higher driving force for forming embedded nanoscale γ precipitates and delay their eventual dissolution when exposed to high temperatures. The low diffusivity of Re in Ni enables γ' coarsening reduction in temperatures higher than 800°C, contingent upon the extent of Re supersaturation at that temperature.

Although the microstructures created by phase separation have promising microstructural stability, there is no known observation of a hierarchical microstructure inducing delay in coarsening of γ' precipitates in any alloy system at temperatures as high as 1000°C. For material applications to capitalize on this enhanced stability, the service temperatures must be conducive to the hierarchical microstructure, less than 800°C in the case of the experimental alloy F-11, in addition to having a proper initial microstructure design with low γ precipitate coarsening. Although hierarchical microstructure has not been reported in cobalt-based γ - γ' alloys, these alloys can potentially exhibit similar microstructure due to their very similarity with Ni-base superalloys.

In conclusion, a combined advanced microscopy and phase-field modeling approach has been used to investigate hierarchical microstructures as a precursor for enhanced coarsening resistance of γ' precipitates in γ - γ' nickel-base alloys. The salient findings are identified below:

- 1) A hierarchical microstructure consisting of nanoscale γ precipitates embedded in γ' precipitates that reside in a continuous γ matrix is observed in an experimental, refractory-containing γ - γ' nickel-base alloy. The embedded γ precipitates remained spherical in nature and did not exhibit directional coalescence, nor did they subdivide the larger γ' precipitate.

2) The supersaturation of Ru, Co, and Re in the γ' phase is responsible for the nucleation of γ precipitates in γ' precipitates and forming a hierarchical microstructure.

3) Phase-field modeling suggests that optimizing γ - γ' hierarchical microstructures for delaying the coarsening may be achieved by targeting a larger initial γ' precipitate radius.

MATERIALS AND METHODS

Alloy processing and thermal treatments

As-cast material of an experimental, high refractory-containing Ni-base superalloy, F-11 (28), was obtained from Sophisticated Alloys Inc. The bulk composition of the as-cast material was measured by Evans Analytical Group using inductively coupled plasma spectroscopy as Ni-13.6Al-7.6Co-1.5W-3Ta-5.9Ru-1.3Re (at %). A homogenization step was applied at 1285°C for 12 hours, followed by air cooling. Air cooling resulted in a varying cooling rate that was initially faster and then slower at lower temperatures. The average cooling rate was approximately 57°C/min between 1285° and 500°C, as shown in fig. S5. The microstructure of the homogenized sample is shown in fig. S6. The homogenized material was then annealed at 700°, 800°, and 1000°C for various times, ranging from 1 to 3000 hours, and subsequently water-quenched.

Microstructural characterization

SEM was conducted using a Quanta 650 field-emission gun (FEG) scanning electron microscope. Samples for TEM were prepared by electropolishing using a solution of 95% methanol and 5% perchloric acid, operated at -30°C with a voltage of 20 to 34 V and current of 25 to 35 mA. TEM analysis was conducted on an FEI Tecnai F30 microscope operated at 300 kV. The γ' precipitate sizes and their associated volume fraction were obtained from analysis of TEM micrographs using ImageJ software. For APT, samples were prepared using the focused ion beam technique on a FEI Quanta 3D FEG dual-beam instrument. Multiple APT experiments were conducted using a local electrode atom probe system (LEAP 4000X HR) from Cameca Instruments. All atom probe experiments were carried out in the voltage evaporation mode at a temperature of 60 K, with an evaporation rate of 0.5%. Subsequent data analysis was performed using IVAS (Integrated Visualization and Analysis Software) 3.6.6 software. Thermodynamic modeling was performed using the CALPHAD (calculation of phase diagrams) (29) method-based software, Thermo-Calc (30), using the TCNi8 database.

Phase-field model and calculation procedure

Here, the Kim-Kim-Suzuki (KKS) phase-field model with parameters based on the Ni-Al system was used to simulate microstructural evolution in a binary Ni-25 Al (at %) alloy with microstructures representative of those observed experimentally in F-11 (31). Because of computational limitations, it was not possible to simulate the full seven-component alloy; however, the physical parameters of the binary alloy could be varied to gain qualitative understanding of how physical parameters affected microstructural evolution. In the KKS model, the microstructure is represented at each position with an order parameter, η , and solute (Al) composition, c . The order parameter value $\eta = 0$ represents the γ phase, and $\eta = 1$ represents the γ' phase, with the interface between phases represented by a continuous variation of η and c . For simulation of the large, noncoalescing γ' particles found in the dendritic region, it is not necessary to distinguish between the four possible types of ordering of the γ' phase relative to the γ phase; thus, a

single order parameter is sufficient to describe the microstructure. The total free energy of the system is then given by

$$F = \int_V \left[[1 - h(\eta)]f_\gamma(c_\gamma) + h(\eta)f_{\gamma'}(c_{\gamma'}) + w\eta^2(1 - \eta)^2 + \frac{\kappa}{2} |\nabla\eta|^2 \right] dV$$

where f_γ and $f_{\gamma'}$ are the free energies of the γ and γ' phases, respectively, c_γ and $c_{\gamma'}$ are the phase compositions of the γ and γ' phases, $h(\eta) = \eta^3(6\eta^2 - 15\eta + 10)$ is an interpolation function that varies smoothly from $h(0) = 0$ to $h(1) = 1$, w is the free energy barrier coefficient, and κ is the gradient energy coefficient. The physical composition c is a function of the phase compositions

$$c = [1 - h(\eta)]c_\gamma + h(\eta)c_{\gamma'}$$

and the chemical potentials (defined with respect to the phase compositions) are constrained to be equal to each other

$$\frac{df_\gamma}{dc_\gamma} = \frac{df_{\gamma'}}{dc_{\gamma'}}$$

The free energy of each phase is the sum of the chemical and elastic energy contributions

$$f_\gamma = f_\gamma^{\text{chem}} + f_\gamma^{\text{el}}, f_{\gamma'} = f_{\gamma'}^{\text{chem}} + f_{\gamma'}^{\text{el}}$$

The chemical energy of each phase is modeled as a parabolic function of composition

$$f_\gamma^{\text{chem}} = \frac{k}{2}(c_\gamma - c_{\gamma,0})^2, f_{\gamma'}^{\text{chem}} = \frac{k}{2}(c_{\gamma'} - c_{\gamma',0})^2$$

with minima at the equilibrium compositions $c_{\gamma,0}$ and $c_{\gamma',0}$ for the aging temperature of 800°C and curvature k set as described in (32). For simulations of the dendritic region, the elastic misfit energy for each phase is given by

$$f_\gamma^{\text{el}} = \frac{1}{2} C_{ijkl}^\gamma \epsilon_{ij} \epsilon_{kl}$$

$$f_{\gamma'}^{\text{el}} = \frac{1}{2} C_{ijkl}^{\gamma'} (\epsilon_{ij} - \epsilon_{ij}^*) (\epsilon_{kl} - \epsilon_{kl}^*)$$

where C_{ijkl}^γ and $C_{ijkl}^{\gamma'}$ are the stiffness tensors, ϵ_{ij} is the total strain tensor, and ϵ_{ij}^* is the misfit strain tensor. To model the system's behavior in time, the concentration evolves by

$$\frac{\partial c}{\partial t} = \nabla \cdot M \nabla \left(\frac{\partial f}{\partial c} \right)$$

where M is the mobility and is given by

$$M = \frac{D}{f_{cc}} = \frac{D}{k}$$

using equations 18 and 29 from (31). The order parameter evolves by the Allen-Cahn equation

$$\frac{\partial \eta}{\partial t} = -L \left(\frac{\delta F}{\delta \eta} \right)$$

where L is the mobility parameter for the interface. Because elastic displacements are assumed to relax much faster than the time scale for chemical diffusion, the mechanical equilibrium equation is solved simultaneously at each time step

$$\nabla \cdot T_{ij} = \nabla \cdot \left[[1 - h(\eta)] T_{ij}^{\gamma} + h(\eta) T_{ij}^{\gamma'} \right] = 0$$

where T_{ij} is the stress tensor and T_{ij}^{γ} and $T_{ij}^{\gamma'}$ are the stress tensors in the respective phases. This approach of interpolating elastic energies and stresses has been described in (33–35). The simulations were conducted in 2D in plane-strain conditions.

The physical and numerical parameters used in the model are listed in table S3. In the KKS model, the interfacial thickness 2λ can be chosen independently of the interfacial energy σ , allowing the use of artificially large 2λ and thereby increasing computational efficiency without affecting the physics of the simulation. Using the relations

$$\sigma = \frac{\sqrt{\kappa w}}{3\sqrt{2}}$$

$$\lambda = \frac{2.2\sqrt{2}}{2} \sqrt{\frac{\kappa}{w}}$$

κ and w were chosen so that $\sigma = 46.8 \text{ mJ/m}^2$ as calculated by ThermoCalc and $2\lambda = 2 \text{ nm}$.

The governing equations were nondimensionalized using length scale $\tilde{L}^* = 1 \text{ nm}$, energy scale $\tilde{E}^* = 2.0 \times 10^9 \text{ J/m}^3$, and time scale $\tilde{\tau}^* = 1.26 \times 10^5 \text{ s}$. The nondimensional equations were discretized using the finite element method, as implemented in the MOOSE (Multiphysics Object Oriented Simulation Environment) framework (36). Linear Lagrange quadrilateral elements with a resolution of $\Delta \mathbf{x} = 0.5$ were used (where overbars indicate dimensionless quantities). The backward Euler scheme was used for time integration with adaptive time steps. The system of equations was solved at each time step using the preconditioned Jacobian-Free Newton-Krylov method.

SUPPLEMENTARY MATERIALS

Supplementary material for this article is available at <http://advances.sciencemag.org/cgi/content/full/4/11/eaao6051/DC1>

Fig. S1. A low-magnification SEM micrograph showing dendritic-interdendritic microstructure in F-11 alloy.

Fig. S2. Coarsening behavior of secondary γ' precipitates in F-11 alloy at 800°C.

Fig. S3. Coarsening behavior of tertiary γ' precipitates in F-11 alloy at 800°C.

Fig. S4. Coarsening kinetics of secondary γ' precipitates in F-11 alloy at 1000°C.

Fig. S5. Air cooling rate curve of F-11 alloy after homogenization at 1285°C for 12 hours.

Fig. S6. A dark-field TEM micrograph of homogenized samples of F-11 alloy shows nucleation of multiple generation of γ' precipitates and no chemical splitting of secondary γ' precipitates.

Fig. S7. Coarsening kinetics of γ precipitates in the γ' matrix in the interdendritic region in F-11 alloy during isothermal annealing at 800°C.

Table S1. Compositions of the γ and γ' phases in the interdendritic and dendritic regions after isothermal annealing at 800°C for 1500 hours.

Table S2. APT estimated composition of the γ' precipitates in the dendritic region after the homogenization heat treatment and after annealing at 800°C for various times.

Table S3. Parameters used for phase-field modeling of the hierarchical microstructure. References (37–41)

REFERENCES AND NOTES

- G. Song, Z. Sun, L. Li, X. Xu, M. Rawlings, C. H. Liebscher, B. Clausen, J. Poplawsky, D. N. Leonard, S. Huang, Z. Teng, C. T. Liu, M. D. Asta, Y. Gao, D. C. Dunand, G. Ghosh, M. Chen, M. E. Fine, P. K. Liaw, Ferritic alloys with extreme creep resistance via coherent hierarchical precipitates. *Sci. Rep.* **5**, 16327 (2015).
- G. Song, Z. Sun, J. D. Poplawsky, X. Xu, M. Chen, P. K. Liaw, Primary and secondary precipitates in a hierarchical-precipitate-strengthened ferritic alloy. *J. Alloys Compd.* **706**, 584–588 (2017).
- A. Devaraj, V. V. Joshi, A. Srivastava, S. Manandhar, V. Moxson, V. A. Duz, C. Lavender, A low-cost hierarchical nanostructured beta-titanium alloy with high strength. *Nat. Commun.* **7**, 11176 (2016).
- F. Vogel, N. Wanderka, Z. Balogh, M. Ibrahim, P. Stender, G. Schmitz, J. Banhart, Mapping the evolution of hierarchical microstructures in a Ni-based superalloy. *Nat. Commun.* **4**, 2955 (2013).
- R. C. Reed, *The Superalloys: Fundamentals and Applications* (Cambridge Univ. Press, 2008).
- F. Tancret, H. K. D. H. Bhadeshia, D. J. C. MacKay, Design of a creep resistant nickel base superalloy for power plant applications: Part 1 - Mechanical properties modelling. *Mater. Sci. Technol.* **19**, 283–290 (2003).
- D. K. Fork, J. Fitch, S. Ziaei, R. I. Jetter, Life estimation of pressurized-air solar-thermal receiver tubes. *J. Sol. Energy Eng.* **134**, 041016 (2012).
- C. T. Sims, N. S. Stoloff, W. C. Hagel, *Superalloys II* (Wiley, 1987).
- T. Maebashi, M. Doi, Coarsening behaviours of coherent γ' and γ precipitates in elastically constrained Ni–Al–Ti alloys. *Mater. Sci. Eng. A* **373**, 72–79 (2004).
- Y. Ma, A. J. Ardell, Coarsening of γ (Ni–Al solid solution) precipitates in a γ' (Ni₃Al) matrix; a striking contrast in behavior from normal γ/γ' alloys. *Scr. Mater.* **52**, 1335–1340 (2005).
- Y. Ma, A. J. Ardell, Coarsening of γ (Ni–Al solid solution) precipitates in a γ' (Ni₃Al) matrix. *Acta Mater.* **55**, 4419–4427 (2007).
- A. J. Ardell, Y. Ma, Coarsening of Ni–Ge solid-solution precipitates in “inverse” Ni₃Ge alloys. *Mater. Sci. Eng. A* **550**, 66–75 (2012).
- M. Doi, D. Miki, T. Moritani, T. Kozakai, Gamma/gamma-prime microstructure formed by phased separation of gamma-prime precipitates in a Ni–Al–Ti alloy, in *Superalloys 2004 (Proceedings of the Tenth International Symposium on Superalloys)* (TMS, 2004), pp. 109–114.
- S. Hata, K. Kimura, H. Gao, S. Matsumura, M. Doi, T. Moritani, J. S. Barnard, J. R. Tong, J. H. Sharp, P. A. Midgley, Electron tomography imaging and analysis of γ' and γ domains in Ni-based superalloys. *Adv. Mater.* **20**, 1905–1909 (2008).
- F. Vogel, N. Wanderka, Z. Balogh, M. Ibrahim, P. Stender, G. Schmitz, T. Fedorova, J. Banhart, Evolution of nanoscale clusters in γ' precipitates of a Ni–Al–Ti model alloy. *UltraMicroscopy* **159** (2), 278–284 (2015).
- J. Boisse, N. Lecoq, R. Patte, H. Zapolsky, Phase-field simulation of coarsening of γ precipitates in an ordered γ' matrix. *Acta Mater.* **55**, 6151–6158 (2007).
- W. Sun, S. Cui, L. Zhang, Y. Du, B. Huang, Phase-field simulation of microstructural evolution of γ precipitate in γ' matrix in binary Ni–Al alloys. *Procedia Eng.* **36**, 200–206 (2012).
- C. Liu, Y. Li, L. Zhu, X. Zhou, Z. Yan, Precipitation kinetics of γ phase in an inverse Ni–Al alloy. *Comput. Condens. Matter* **11**, 40–46 (2017).
- M. Durand-Chare, *The Microstructure of Superalloys* (Routledge, 1997).
- N. Warnken, Studies on the solidification path of single crystal superalloys. *J. Phase Equilib. Diff.* **37**, 100–107 (2016).
- J. S. Van Sluytman, C. J. Mocer, T. M. Pollock, A Pt-modified Ni-base superalloy with high temperature precipitate stability. *Mater. Sci. Eng. A* **639**, 747–754 (2015).
- C. H. Su, P. W. Voorhees, The dynamics of precipitate evolution in elastically stressed solids—I. Inverse coarsening. *Acta Mater.* **44**, 1987–1999 (1996).
- A. J. Ardell, Interfacial free energies and solute diffusivities from data on Ostwald ripening. *Interface Sci.* **3**, 119–125 (1995).
- D. A. Porter, K. E. Easterling, M. Sherif, *Phase Transformations in Metals and Alloys* (Taylor & Francis, ed. 3, 2009).
- T. Pretorius, D. Baither, E. Nembach, Strengthening of an L1₂-ordered γ' -intermetallic by disordered γ -particles. Part II: Measurements of the CRSS and TEM observations of dislocation processes in Ni₆₀Co₉Al₁₈Ti₄. *Acta Mater.* **49**, 1981–1985 (2001).
- A. J. Ardell, M. Pozuelo, Disorder strengthening of ordered L1₂ alloys by face centered cubic (A1) precipitates. *Intermetallics* **88**, 81–90 (2017).
- K. E. Yoon, R. D. Noebe, D. N. Seidman, Effects of rhenium addition on the temporal evolution of the nanostructure and chemistry of a model Ni–Cr–Al superalloy. II: Analysis of the coarsening behavior. *Acta Mater.* **55**, 1159–1169 (2007).

28. L. J. Carroll, Q. Feng, J. F. Mansfield, T. M. Pollock, Elemental partitioning in Ru-containing nickel-base single crystal superalloys. *Mater. Sci. Eng. A* **457**, 292–299 (2007).
29. L. Kaufman, H. Bernstein, *Computer Calculation of Phase Diagrams with Special Reference to Refractory Metals* (Academic Press, 1970).
30. J.-O. Andersson, T. Helander, L. Höglund, P. Shi, B. Sundman, Thermo-Calc & DICTRA, computational tools for materials science. *Calphad* **26**, 273–312 (2002).
31. S. G. Kim, W. T. Kim, T. Suzuki, Phase-field model for binary alloys. *Phys. Rev. E* **60**, 7186–7197 (1999).
32. J. Zhu, thesis, Pennsylvania State University (2002).
33. K. Ammar, B. Appolaire, G. Cailletaud, S. Forest, Combining phase-field approach and homogenization methods for modelling phase transformation in elastoplastic media. *Eur. J. Comput. Mech.* **18**, 485–523 (2009).
34. A. Durga, P. Wollants, N. Moelans, Evaluation of interfacial excess contributions in different phase-field models for elastically inhomogeneous systems. *Model. Simul. Mater. Sci. Eng.* **21**, 055018 (2013).
35. A. Durga, P. Wollants, N. Moelans, A quantitative phase-field model for two-phase elastically inhomogeneous systems. *Comput. Mater. Sci.* **99**, 81–95 (2015).
36. D. Gaston, C. Newman, G. Hansen, D. Lebrun-Grandié, MOOSE: A parallel computational framework for coupled systems of nonlinear equations. *Nucl. Eng. Des.* **239**, 1768–1778 (2009).
37. H. A. Calderon, P. W. Voorhees, J. L. Murray, G. Kosterz, Ostwald ripening in concentrated alloys. *Acta Metall.* **42**, 991–1000 (1994).
38. N. Dupin, I. Ansara, B. Sundman, Thermodynamic re-assessment of the ternary system Al-Cr-Ni. *Calphad* **25** (2), 279–298 (2001).
39. S. V. Prikhodko, J. D. Carnes, D. G. Isaak, A. J. Ardell, Elastic constants of a Ni-12.69 AT. % Al alloy from 295 to 1300 K. *Scr. Mater.* **38**, 67–72 (1997).
40. S. V. Prikhodko, H. Yang, A. J. Ardell, J. D. Carnes, D. G. Isaak, Temperature and composition dependence of the elastic constants of Ni₃Al. *Metall. Mater. Trans.* **30**, 2403–2408 (1999).
41. A. B. Kamara, A. J. Ardell, C. N. J. Wagner, Lattice misfits in four binary Ni-Base γ/γ' alloys at ambient and elevated temperatures. *Metall. Mater. Trans.* **27**, 2888–2896 (1996).

Acknowledgments: We would like to thank W. D. Swank and D. C. Haggard for the extensive assistance with the experimental work throughout the course of this study. APT and TEM work was carried out at the Center for Advanced Energy Studies–Microscopy and Characterization Suite (CAES-MaCS). **Funding:** This work has been supported through the Idaho National Laboratory (INL) Laboratory Directed Research and Development (LDRD) Program under U.S. Department of Energy (DOE) Idaho Operations Office contract no. DE-AC07-05ID14517. This manuscript has been authored by Battelle Energy Alliance LLC under contract no. DE-AC07-05ID14517 with the DOE. The U.S. Government retains and the publisher, by accepting the article for publication, acknowledges that the U.S. Government retains a nonexclusive, paid-up, irrevocable, worldwide license to publish or reproduce the published form of this manuscript, or allow others to do so, for U.S. Government purposes. **Author contributions:** S.M., M.C.C., T.M.P., and L.J.C. generated the idea and designed experiments. S.M. performed TEM and analyzed the results. L.K.A. performed phase-field modeling. All the authors discussed and contributed to the manuscript. **Competing interests:** The authors declare that they have no competing interests. **Data and materials availability:** All data needed to evaluate the conclusions in the paper are present in the paper and/or the Supplementary Materials. Additional data related to this paper may be requested from the authors.

Submitted 12 June 2018
Accepted 19 October 2018
Published 16 November 2018
10.1126/sciadv.aa06051

Citation: S. Meher, L. K. Aagesen, M. C. Carroll, T. M. Pollock, L. J. Carroll, The origin and stability of nanostructural hierarchy in crystalline solids. *Sci. Adv.* **4**, ea06051 (2018).